

On the Thermal Signature of the Residual Foam in Breaking Waves

Naeem Masnadi^{1,1}, C Christopher Chickadel^{1,1}, and Andrew Jessup^{2,2}

¹University of Washington

²University of Washington, USA

November 30, 2022

Abstract

Quantifying energy dissipation due to wave breaking remains an essential but elusive goal for studying and modeling air-sea fluxes of heat, gas, and momentum. Previous observations have shown that lifetimes of bubble plumes and surface foam are directly related to the dissipated energy. Specifically, the foam decay time can be used to estimate the timescale of the subsurface bubble plume and the energy dissipated in the breaking process. A mitigating factor is that the foam decay time can be significantly affected by the surfactant concentration. Here we present an experimental investigation of a new technique that exploits the thermal signature of cooling foam to infer wave breaking dynamics. The experiments were conducted in a laboratory wave tank using artificial seawater with and without the addition of a surfactant. We show that the time from the start of the breaking process to the onset of cooling scales with the bubble plume decay time and the dissipated energy, and is not significantly affected by the presence of additional surfactants. We confirm observations from the field of the spatial variability of the temperature of foam generated by an individual breaking event, which has implications for inferring the spatial variability of bubble plume depth.

On the Thermal Signature of the Residual Foam in Breaking Waves

Naeem Masnadi, C. Chris Chickadel, and Andrew T. Jessup¹

¹Applied Physics Lab, University of Washington

Key Points:

- The thermal signature of cooling residual foam can be used to infer breaking wave dynamics.
- The time from the start of the breaking process to when the residual foam begins to cool scales with the bubble plume decay time.
- The cooling time of the foam is not significantly affected by the presence of surfactants.

Corresponding author: C. Chris Chickadel, chickadel@apl.washington.edu

Abstract

Quantifying energy dissipation due to wave breaking remains an essential but elusive goal for studying and modeling air-sea fluxes of heat, gas, and momentum. Previous observations have shown that lifetimes of bubble plumes and surface foam are directly related to the dissipated energy. Specifically, the foam decay time can be used to estimate the timescale of the subsurface bubble plume and the energy dissipated in the breaking process. A mitigating factor is that the foam decay time can be significantly affected by the surfactant concentration. Here we present an experimental investigation of a new technique that exploits the thermal signature of cooling foam to infer wave breaking dynamics. The experiments were conducted in a laboratory wave tank using artificial seawater with and without the addition of a surfactant. We show that the time from the start of the breaking process to the onset of cooling scales with the bubble plume decay time and the dissipated energy, and is not significantly affected by the presence of additional surfactants. We confirm observations from the field of the spatial variability of the temperature of foam generated by an individual breaking event, which has implications for inferring the spatial variability of bubble plume depth.

Plain Language Summary

Breaking waves cause mixing and are important for redistributing heat, transporting gases between the air and the water, and generating currents. Bubbles from breaking waves eventually rise and stay at the surface where they can be visually seen as foam. Scientists have found that the time it takes for the foam to disappear is related to the strength of the breaking waves. However, natural chemicals in the seawater can cause the bubbles to disappear more slowly, increasing the time they are seen at the surface. We present a new method to estimate when the bubble plume has decayed based on the foam temperature. We generate breaking waves in a laboratory and use an infrared camera to measure the temperature of the foam and find that the foam cools when bubbles stop rising. We varied the strength of the breaking waves and measured the cooling time for the foam to show that larger, stronger breaking waves cause a longer time before the foam begins to cool. When we added chemicals to increase the time foam stays at the surface, the cooling time remains about the same, even though the foam is still seen at the surface for a longer time.

1 Introduction

Wave breaking plays a critical role in air-sea interaction processes in both the open ocean and the surf zone. The energy transferred from the atmosphere to the ocean through wind-wave generation is ultimately dissipated by wave breaking. Therefore, quantifying the energy dissipation due to wave breaking is directly relevant to wave prediction models used for operational sea-state forecasting and the impact of waves on coastal regions. At high wind speeds, bubbles generated by large scale breaking waves are the primary mechanism for gas transfer and dominate the energy dissipation due to breaking (Lamarre & Melville, 1991). Bubbles generated by breaking waves also contribute to marine aerosol formation through spray droplets produced when foam bubbles burst at the surface (Veron, 2015; Erinin et al., 2019, and references therein). Foam generated by wave breaking has increased reflectivity of solar radiation that can affect the earth’s albedo (Evans et al., 2010; Gordon & Jacobs, 1977) and the enhanced microwave emissivity of foam impacts space-borne radiometer measurements of wind speed. In short, wave breaking is an important mechanism for fluxes of momentum, gas, and heat across the air-water interface and for global ocean remote sensing applications. Here we focus on breaking waves that produce visible foam.

A wave begins to break when the forward face steepens and the crest becomes unstable. The morphology of an individual breaking wave that generates foam is generally categorized as either spilling or plunging. Plunging breakers occur when a wave crest forms an open curl and rapidly falls forward. Spilling breakers are characterized by a wave crest that spills

forward and rolls down the face. For both types, subsurface bubble plumes are generated by the impact of the overturning crest on the water surface. For plunging breakers, bubbles are also injected when the air pocket formed by the curling crest collapses, and by the jet impinging on the surface (Kiger & Duncan, 2012). As the actively breaking crest continues to propagate for the breaker lifetime, a bubbly turbulent wake is left behind. Bubbles rise to the surface and produce patches of residual surface foam as turbulence in the wake subsides.

The term whitecap has been used to describe both the foam generated by the actively breaking crest and the residual foam left behind in the wake. Monahan and Lu (1990) denoted the actively breaking period as stage-A and the period following as stage-B. Stage-A also has been referred to as the “acoustically active” period (Deane & Stokes, 2002), because the formation and fragmentation of bubbles generate underwater sound during this period. Stage-A includes the formation of the actively breaking crest and creation of the bubble plume and ends when air is no longer actively entrained. Stage-B includes the expansion and rise of the bubble plume as well as the formation and decay of the resulting residual foam and typically is of longer duration than stage-A (Kleiss & Melville, 2010; Monahan & Lu, 1990).

Whitecap coverage, W , is the percentage area of the sea surface covered by foam measured from visible imagery. Techniques for measuring W have evolved from labor-intensive analysis of individual photographs (Monahan, 1969) to automated techniques using high-resolution digital imagery (Callaghan & White, 2009). Scanlon and Ward (2013) recently reported on a manual technique to separate active and maturing whitecaps, but automated processing of visible imagery remains a challenge. Most visible measurements of W include both stages of whitecap foam because of the difficulty of objectively and automatically distinguishing between stage-A and stage-B foam. However, there is strong motivation to be able to separately measure whitecap coverage for stage-A, W_A , and for stage-B, W_B , in order to examine the different processes of interest that are associated with the different stages. For instance, W_A is the appropriate coverage to determine the breaking rate and for correlation with the energy dissipation (Kleiss & Melville, 2010) while W_B has been related to sea-salt aerosol production due to the preponderance of bursting bubbles as the foam dissipates (Callaghan, 2013; Monahan et al., 1986).

Since wave breaking is driven by wind stress, many authors have pursued a fundamental parameterization of W with wind speed. A compilation of historical data sets by Angelova and Webster (2006) shows scatter of W versus wind speed of over three orders of magnitude, suggesting other factors need to be considered. Recent results by Callaghan et al. (2008, 2012, 2013) indicate that potential contributors to the observed scatter of W with wind speed include environmental parameters such as wave field characteristics, breaker type, and surfactant effects as well as differences in image acquisition and analysis techniques. Variations in the decay time of oceanic whitecap foam led Callaghan et al. (2012) to speculate that the two primary mechanisms that cause scatter of whitecap coverage with wind speed are (i) the effect of surfactants on foam stability and (ii) differences between bubble plume characteristics caused by variation in breaker type.

In the laboratory, Callaghan et al. (2013) investigated these two mechanisms by comparing the visible decay times for foam, τ_{foam} , and for the bubble plume, τ_{plume} , for whitecaps generated by focused wave packets using clean and surfactant-contaminated (Triton X-100 at $204 \mu\text{gr}\cdot\text{L}^{-1}$) seawater. They found that τ_{plume} was proportional to the increase in energy dissipated as the scale of breaking ranged from spilling to plunging. However, when surfactants were present, the scaling between τ_{foam} and τ_{plume} varied significantly. Surfactants act to stabilize the bubbles, causing them to persist at the surface after the bubble plume has decayed and the foam generation process has ceased. For clean conditions, the foam decay time can provide a direct estimate of the plume degassing time. In the presence of surfactants, their effect on increasing the foam decay time needs to be accounted for in order to infer the plume decay time (Callaghan et al., 2017).

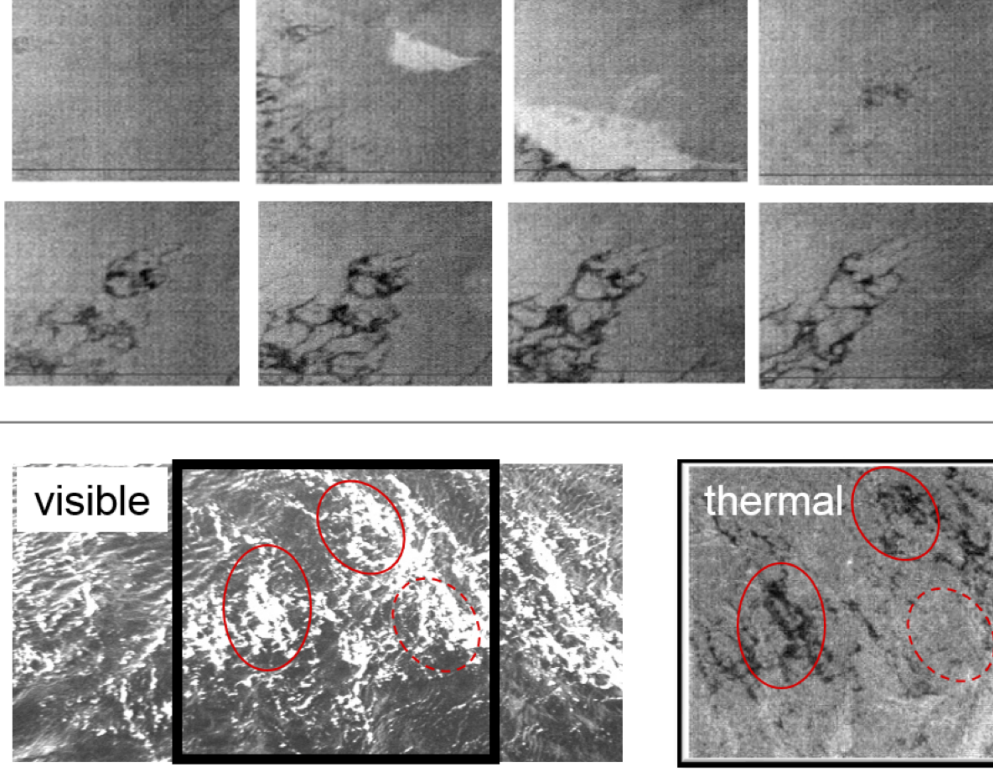


Figure 1. (Top) An examples of infrared image sequences showing the cooling of residual foam in the wake of a breaking wave in the open ocean. Time increases left to right then top to bottom. Lighter shades of gray are warm and darker shades are cold. Image size is approximately $5 \text{ m} \times 5 \text{ m}$. (Bottom) Simultaneous visible (left) and infrared (right) images of residual foam in the wake of a breaking wave in the open ocean. Solid ovals indicate locations where visible foam appears cool while foam does not appear cool in the dashed oval (Fogelberg, 2003).

The infrared image sequence in Figure 1 illustrates the rapid cooling of foam left behind after the passage of a breaking wave, similar to observations reported by Fogelberg (2003) and Marmorino and Smith (2005). Recent laboratory findings by Chickadel et al. (2014) that the heat flux from foam is three to four times greater than foam-free water are consistent with the suggestion by Marmorino and Smith (2005) that the cooling is due to enhanced evaporation from bubbles. Chickadel et al. (2014) also reported that the foam cooling begins after the foam-producing bubbles cease rising. The foam cooling phenomenon has been used recently to distinguish between the active and residual foam. In the open ocean, Potter et al. (2015) used infrared imagery to quantify the lifetime stages and characterize properties of the active and residual whitecaps. In the surf zone, Carini et al. (2015) used the difference in the thermal signature of active and residual foam to identify and extract the perpendicular crest length of the aerated breaking region.

A consistent observation in the field is that there is a momentary delay of $O(1 \text{ s})$ between when the foam appears in the visible and when it appears cool in the infrared. The foam is generated by air entrainment and bubbles at the surface so its initial temperature will be approximately the same as that of the surface water. As the breaking process continues, the surface foam is replenished from below by bubbles rising to the surface from the plume.

Since the heat flux for foam is three to four times greater than that for foam-free water, the delay in the appearance of cool foam implies that the surface of the foam is replenished by near-surface water from below at a rate such that there is not enough time for it to cool. That is, the rate of replenishment of the foam overcomes the cooling rate. As the bubble plume decays and the foam replenishment rate lessens, the foam will begin to cool and its temperature will drop. Thus the time between the onset of breaking and the appearance of cool foam should be related to the timescale of the bubble plume decay. Additionally, field observations show that not all residual foam from a given breaking event begins to cool at the same time. The simultaneous visible and infrared images in Figure 1(bottom) show two regions outlined by solid ovals where foam is cooler than the undisturbed surface while in the dashed oval region the foam temperature is comparable to the undisturbed surface. Since the foam in Figure 1(bottom) was generated at the same time, the delay in the onset of cooling at different locations implies that the bubble plume depth was greater for the location with longer onset times.

Here we seek to exploit the thermal signature of the cooling of surface foam in the wake of a breaking wave to infer subsurface plume dynamics. Our long-term goal is to develop a new remote sensing technique that will simultaneously provide (1) a measurement of the bubble plume timescale relevant to estimating dissipation and (2) a map of the spatial variability of the bubble plume depth. Thus our objectives are to test the following two hypotheses:

1. The time from the start of breaking to the onset of foam cooling scales with the bubble plume decay time.
2. For an individual breaking event, the spatial variability of the bubble plume depth can be inferred by the spatial variability of the time for the onset of foam cooling.

With regard to Hypothesis (1), we seek to show that while the foam at the surface is being replenished from below, its temperature remains comparable to that of the water from which it is generated. The cooling begins only when the rate of replenishment by the rising bubbles is less than the foam cooling rate. The start of the cooling is delayed for more energetic breaking waves that generate larger and deeper bubble plumes compared to less energetic breakers that generate smaller and shallower plumes. With regard to Hypothesis (2), we seek to confirm in the laboratory the observations from the field of the spatial variability of the temperature of foam generated at the same time by an individual breaking event. A complete test of Hypothesis (2) requires subsurface measurement of the spatial variability of bubble plume depth and size distribution, which is beyond the scope of this effort. However, the spatial variability of the surface foam temperature can be observed in infrared imagery.

We present a new approach for estimating the timescale of the subsurface bubble plume based on the timescale of the cooling foam. The results from our laboratory experiments show that the onset of cooling of the foam scales with a measure of the decay time of the bubble plume and that the cooling onset time varies spatially for foam simultaneously generated by an individual event. The cooling time is not significantly affected by surfactants, which is in contrast to the finding that foam persist longer when surfactants are present (Callaghan et al., 2013). We demonstrate that infrared imagery can provide the ability to infer the bubble plume decay time and thus provide a measure of wave energy dissipation. We also confirm in the laboratory the observations from the field of the spatial variability of the temperature of foam generated at the same time by an individual breaking event.

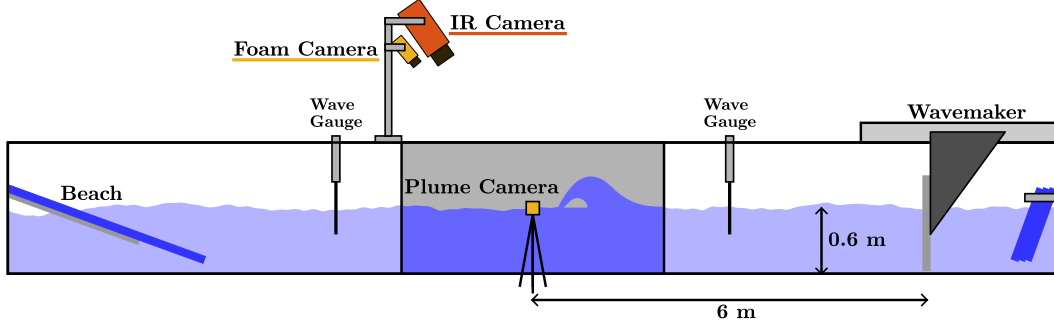


Figure 2. Schematic of the experimental setup. One side wall of the tank is made of glass for optical access. The other side wall is painted black in a 1.6 m long test section. The top of the tank is covered except for the test section. The waves are designed to break at a location approximately 6 m from the wave paddle. The tank width is 0.91 m.

2 Experimental Details

2.1 Setup

The experiments were performed in the Washington Air-Sea Interaction Research Facility (WASIRF) wave flume at the University of Washington (Figure 2). The wave flume is 12 m long, 0.91 m wide, and 1.2 m tall, with one side wall made of glass that allows optical access. The top of the tank was covered with removable panels except for the test section that was left open for imaging. The facility includes a water circulation system that is equipped with an inline filter and electric heater. The flume was filled with salt water to a depth of 0.6 m using Instant Ocean and tap water. The salinity was set to 30 ppt and was frequently checked with a refractometer to ensure it remained constant during the experiments.

A programmable piston-type wavemaker at one end of the tank was used to generate breaking waves. The wavemaker consists of a flat rectangular paddle that is 0.9 m tall and spans the tank width and extends to the bottom of the tank. The motion of the wavemaker is controlled by an analog signal sent to the controller of the servo motor. Wave absorbing beaches were installed at both ends of the tank to diminish wave reflection from the end walls.

2.2 Wave Generation

Breaking waves are generated using the dispersive focusing wave packet technique used extensively in laboratory experiments (Rapp & Melville, 1990; Duncan et al., 1999; Drazen et al., 2008; Wang et al., 2018). In this technique, a packet is composed of many components and is designed such that all the components have the same phase at a prescribed “breaking” location. In the experiments presented here, the motion of the wavemaker can be described as

$$\eta_0 = \sum_{i=1}^N \frac{a_i}{a_i^{corr}} \cos(-k_i x_b - 2\pi f_i(t - t_b) - \phi_i^{corr}) \quad (1)$$

where η_0 is the wavemaker horizontal displacement, $N = 32$ is the total number of components, and for each component, a_i is the amplitude, a_i^{corr} is the amplitude correction factor found in the calibration process, k_i is the wavenumber, f_i is the frequency, and ϕ_i^{corr} is the phase correction. x_b and t_b are the theoretical breaking location and time, respectively. Equation (1) produces a periodic signal and needs to be windowed to provide the proper wavemaker motion. We used a window with hyperbolic tangent edges to taper the signal

in a smooth fashion. The parameters that control the shape of the wave packet signal and the breaking location of the waves are the central frequency of the packet, $f_c = 0.88$ Hz, the frequency bandwidth, $\Delta f = 0.5f_c$, and the normalized breaking location, $x_b k_c = 33$, where k_c is the wavenumber corresponding to the central frequency. These parameters were chosen to generate breaking waves with similar shape but with considerable difference in foam generation, plume depth, and energy dissipation. The global slope of a wave packet is used as the control parameter for the scale of the breaking waves and is defined as:

$$S = \sum_{i=1}^N a_i k_i \quad (2)$$

Following Loewen (1991), all the components in the wave packet are chosen to have the same slope. Hence, increasing the global slope, S , is essentially equivalent to multiplying the signal by a constant factor without changing the overall shape.

2.3 Measurement Techniques

The bubble plume and the surface foam generated by breaking waves were measured using two identical visible cameras (Point Grey model Blackfly; 4 MP, 15 fps) to visualize the light scattered by the bubbles against the dark background in the test section, which was illuminated by two LED light sources. The bubble plume camera was located outside the glass side wall of the tank and was oriented normal to the wall. The horizontal center-line of the field of view coincided with the calm water surface. The field of view of this camera was approximately $1.2 \text{ m} \times 1.2 \text{ m}$. The foam camera was located approximately 2 m above the water surface and viewed the surface at an incidence angle of 30 degrees. The field of view of this camera extended to regions outside of the tank and these regions were masked in the analysis.

The surface temperature was measured using an uncooled, longwave (7-14 μm) infrared camera (DRS model UC640; 640×480 pixels, 30 fps, NEDT 25 mK) that was mounted adjacent to the foam camera. The foam and infrared cameras had overlapping fields of view and a transformation map between the two cameras was found in the calibration process. A circular metal target was attached to a float on the water surface and heated before being placed inside the tank so it would be visible to the infrared camera. The target was then moved in different parts of the field of view and imaged by the two cameras simultaneously. The center of the circular target was tracked through the image sequences and the transformation between the two cameras was found using a projective transformation between the pairs of target locations (Goshtasby, 1986). A second transformation was found and applied to all infrared and visible images to account for the oblique perspective of these cameras.

The two visible cameras and the infrared camera were time-synchronized through the data collection software to record the breaking process simultaneously. Two capacitance-type wire wave gauges were mounted approximately 1.5 m upstream and downstream of the breaking location. The surface elevation data recorded at these locations were used to estimate the total energy dissipated by the breakers (Rapp & Melville, 1990).

2.4 Experimental Procedures and Conditions

For the experiments presented here, four breakers with slope values of $S = 0.34, 0.35, 0.36$, and 0.37 were used. This range of slopes corresponds to plunging breakers that vary in intensity, amount of air entrained, and energy dissipation. This range of slopes corresponds to a range of $E = 74\text{-}105 \text{ J/m}$ (along the crest of wave) in energy dissipation. Properties of the breakers are listed in Table 1.

The data collection process was automated so that many runs could be carried out unattended. The water in the tank was recirculated and filtered the night before each experiment day for about eight hours. In the morning of each experiment day, the water was

Table 1. Properties of the breaking waves used in the experiments where d_{\max} is the maximum depth of the bubble plume, ΔE is the total energy dissipation as estimated by upstream and downstream wave gauges, A_{plume}^{\max} is the maximum plume area, and A_{foam}^{\max} is the maximum whitecap area.

Slope	0.34	0.35	0.36	0.37
ΔE (J/m)	73.93	85.23	93.69	105.03
d_{\max} (cm)	15.05 ± 1.64	18.48 ± 1.71	24.79 ± 2.98	29.12 ± 3.21
A_{plume}^{\max} (m ²)	0.085 ± 0.0066	0.113 ± 0.0079	0.141 ± 0.0081	0.158 ± 0.0105
A_{foam}^{\max} (m ²)	0.599 ± 0.038	0.728 ± 0.045	0.808 ± 0.065	0.864 ± 0.058

heated to approximately 1 degree Celsius above the ambient air temperature. The air temperature varied slightly during the experiments due to the diurnal cycle. The temperature difference, $\Delta T = T_{\text{water}} - T_{\text{air}}$, was in the range of zero to 2 °C for all the experimental runs presented here. The wavemaker and the data collection computers were set up to continuously generate breaking waves and collect data every ten minutes over the course of the day. This time between runs was found to be sufficient for the wave reflections to dissipate.

Two sets of experiments were carried out; in the first set, clean salt water was used (no additional surfactants), and in the second set, Triton X-100 was added to achieve a concentration of 200 $\mu\text{g/L}$. For each wave slope and for a condition with or without additional surfactants (eight total cases), between 50 to 60 runs were recorded and analyzed for a total of 462 individual breaking waves overall.

3 Image Processing

A sequence of visible bubble plume and foam images for a breaker propagating from left to right are shown in Figure 3 (see the supplementary material for movies corresponding to the image sequences). The images are separated by $\Delta t = 1/3$ s and the first image in the sequence is from $t = 1/3$ s. The time origin, $t = 0$, denotes the start of the breaking process and is found by manually inspecting the bubble plume camera images. For the example shown in Figure 3 (top), which is the largest wave slope used, a significant amount of air is entrained and left behind by the active breaker in (a) and (b). Two relatively large and distinct bubble plumes occur for this breaker, as seen in images (c) and (d). The bubbles quickly rise to the surface in (e) and (f), and the residual surface foam left behind is apparent in (g) and (h).

The gray-scale visible images shown in Figure 3 were analyzed to obtain foam and plume area time series. First, the background was subtracted from all images in a sequence to enhance the signal and reduce the effect of non-uniformity in the lighting condition. Then, a manually determined intensity threshold was applied to segregate the bright foam and bubbles from the dark background, resulting in black and white (B/W) image masks. The threshold was chosen to include all visible foam and bubbles, regardless of size or brightness. The same fixed threshold was used for all the runs since the lighting conditions were invariant. For the foam images, bright regions smaller than 200 pixels were removed from the images to reduce the speckle noise. Dark areas smaller than 200 pixels that are enclosed by bright foam were converted to white pixels. These regions are typically centers of large bubbles before they burst at the surface. The foam images were then transformed into the coordinate system of the infrared camera. A sequence of the resulting B/W bubble plume and foam masks is shown in Figure 4. This processing was done in the range of $t = -1$ s to $t = 10$ s for each run (166 frames per run).

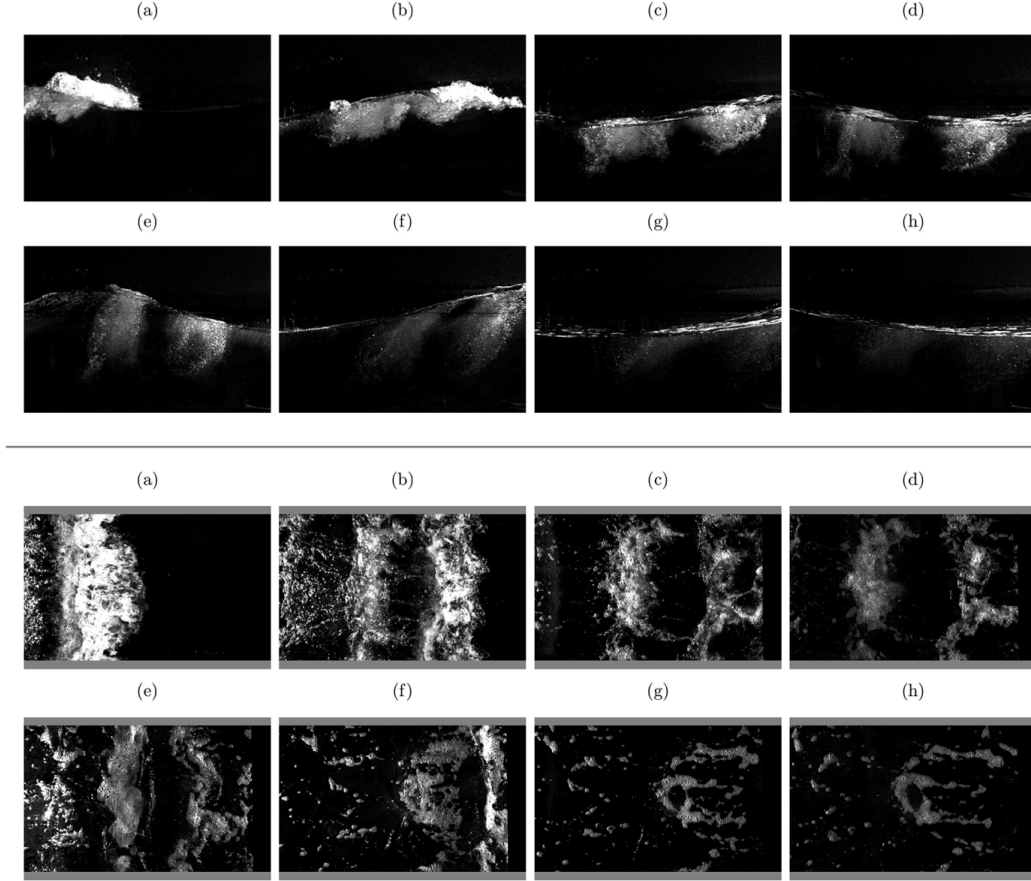


Figure 3. A sequence of visible images of a breaking wave with a slope of $S = 0.37$. The wave is propagating from left to right. The frames are separated in time by $1/3$ s. The wave packets are designed so that the breaking occurs at the edge of the field of view. (Top) bubble plume images taken from the camera that is looking through the glass wall of the tank. (Bottom) visible foam images taken by the camera that is looking down at the water surface. The foam images are shown in the coordinate system of the infrared camera images (see text). Each image is approximately 1.2 m long. This figure corresponds to Movie S2 in the supplementary information.

The sequence of infrared images of the surface in Figures 5 are from the individual run corresponding to the visible imagery in Figures 3 and 4. The blue lines are the boundaries of the regions covered by the visible foam and are derived from the masks in Figure 4. The images show the temperature anomaly, defined as the difference between the instantaneous temperature and the background reference temperature. The background reference temperature for each individual run was the maximum value of the spatially-averaged temperature of the field in the time span of $0 < t < 10$ s. The temperature range is shown in the colorbar with dark corresponding to cold and bright to warm.

At the beginning of the breaking process, the cool skin layer is destroyed so that the skin temperature during breaking and in the wake is approximately equal to the bulk temperature (Jessup et al., 1997). As the crest begins breaking in Figure 5(a), the nearly uniform disruption of the cool skin layer produces a front of warm foam over the entire width of the tank that advances with the crest. In frames (a)-(c), the temperature of the surface disrupted by the breaking crest is nearly uniform, regardless of whether it is foam-covered or

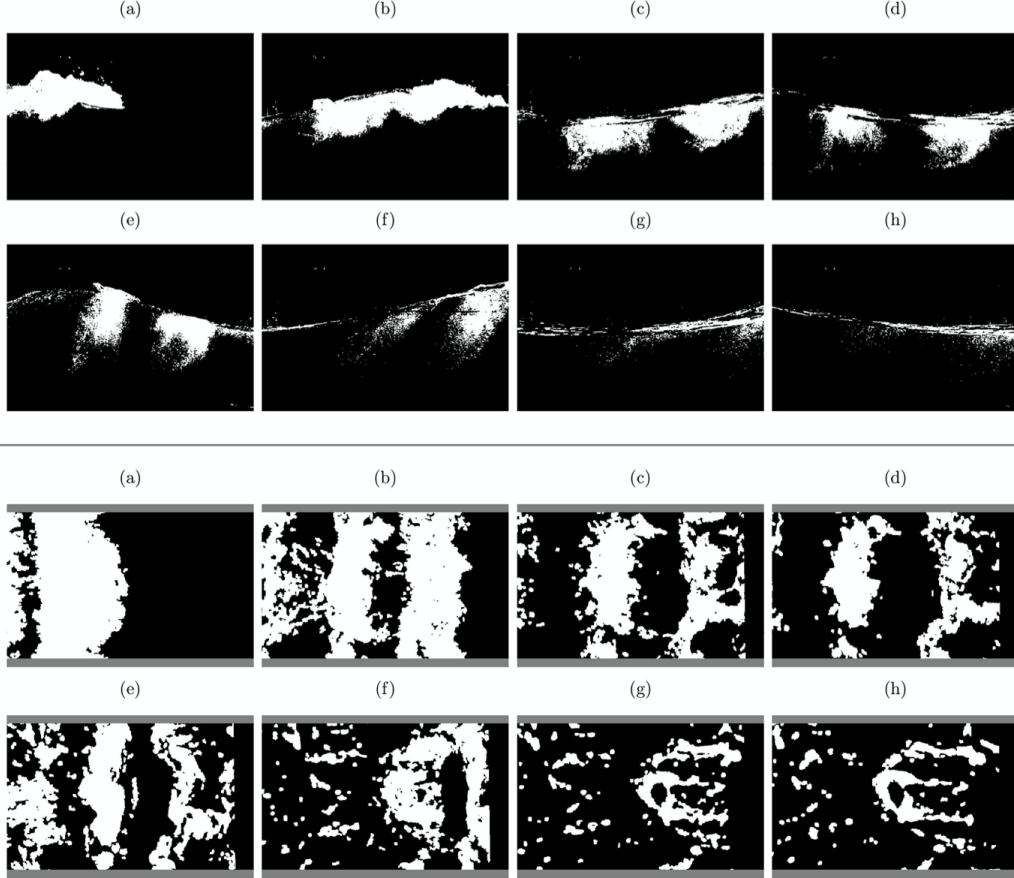


Figure 4. A sequence of thresholded B/W images of a breaking wave with a slope of $S = 0.37$ corresponding to the images in Figure 3.

foam-free. The foam begins to cool in (d) but the degree of cooling is not spatially uniform over the foam until the end of the sequence in (g)-(h). This spatial variation is apparent between the two main foam regions in (d) and (e). Eventually, the foam dissipates and after several minutes (not shown in the figure), the cool skin layer recovers and the surface temperature drops to its value before the disruption by the breaking wave.

The image sequences of the surface foam and bubble plume in Figures 3 and 4 and the foam temperature anomaly in Figure 5 are consistent with the conceptual relationship presented in the discussion of Figure 1 (bottom). That is, while the surface foam is being renewed by rising bubbles from below during the active breaking process, its temperature is comparable to that of the surrounding foam-free water. As the bubble plume decays and the renewal rate decreases, the enhanced heat flux of the foam causes its temperature to drop. A schematic representation of the conceptual relationship between the foam or bubble plume area and foam temperature anomaly is illustrated in Figure 6. The area exhibits a growth phase, characterized by a rapid increase from when breaking begins at $t = 0$ to a maximum, followed by a decay phase of varying duration. The foam temperature anomaly also increases rapidly from $t = 0$ but remains elevated for some finite time until the renewal of the foam from below is reduced to the point where it no longer inhibits the cooling. The primary time variables used in our analysis shown in the figure are: t_{cool} , the time from $t = 0$ to the onset of foam cooling; t_{max} , the time from $t = 0$ to the maximum area; and

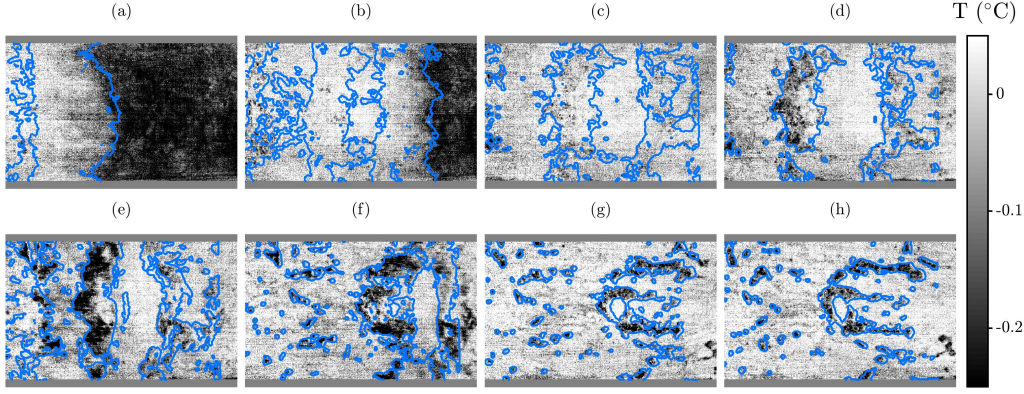


Figure 5. A sequence of infrared images of the surface temperature anomaly corresponding to the images in Figure 3. The temperature range is shown in the colorbar with dark meaning cold and bright meaning warm. The blue outlines show the location of the foam extracted from the visible foam images (Figure 4). This figure corresponds to Movie S2 in the supplementary information.

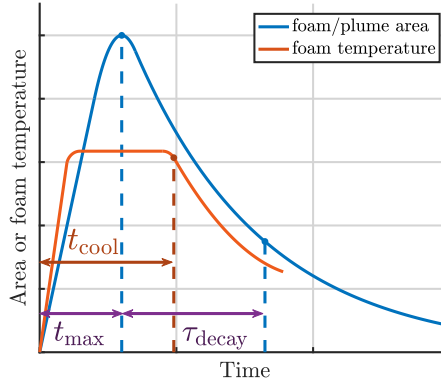


Figure 6. Schematic representation of conceptual relationship between the foam or bubble plume area (blue) and the foam temperature (orange) showing relevant time variables: t_{cool} , the time from $t = 0$ to the onset of foam cooling; t_{max} , the time from $t = 0$ to the maximum area; and τ_{decay} , the area decay timescale equal to the e-folding time of the decay from the maximum area. The total bubble plume timescale (not shown) is defined as $\tau_{\text{plume}}^{\text{total}} = t_{\text{plume}}^{\text{max}} + \tau_{\text{plume}}^{\text{decay}}$.

τ_{decay} , the area decay timescale equal to the e-folding time of the decay from the maximum area. The total bubble plume timescale (not shown) is defined as $\tau_{\text{plume}}^{\text{total}} = t_{\text{plume}}^{\text{max}} + \tau_{\text{plume}}^{\text{decay}}$.

4 Results and Discussion

The B/W masks in Figure 4 were used to calculate the foam and bubble plume areas. The foam coverage is defined as the fraction of the image area that is covered by the foam in each B/W mask. The bubble plume area was similarly extracted from the B/W bubble plume masks. In each plot of foam and bubble plume area time series shown in Figure 7, the thick lines are the ensemble averages for each condition (slope and surfactant) and the shaded areas show one standard deviation of the samples. Both the foam and bubble plume areas exhibit a growth and decay phase as illustrated in Figure 6.

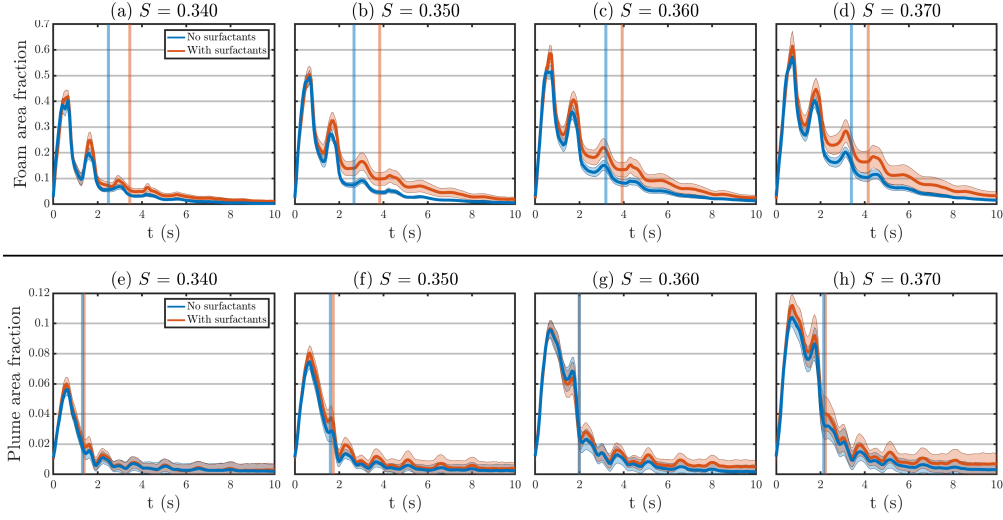


Figure 7. Time series of the foam area (top) and the bubble plume cross-sectional area (bottom). The area is normalized by the image size. The thick lines are the ensemble averages for each condition (slope and surfactant) and the shaded areas show one standard deviations of the samples. The vertical lines indicate the location of the e-folding time from the maximum relative to time $t=0$.

Figure 7(a-d) shows the time series of the foam coverage for each wave packet. The oscillations in the foam and the bubble plume coverage during the decay phase and the existence of local peaks in the time series are due to the orbital motion of the surface waves which causes the surface foam and the bubble plume to expand and contract, and be advected in and out of the field of view. The amount of foam generated by the breaking waves increases with the slope of the wave packet. Initially, there is little difference between clean water and surfactant-added cases. However, the longevity of the foam is increased for the cases with additional surfactants, as is apparent from the foam coverage values at later times. Furthermore, there is more variation in the amount of foam among individual runs with the same experimental condition for the cases with additional surfactants, especially at later times.

The time series of the bubble plume area are shown in Figure 7(e-h). Similar to the foam coverage, the maximum bubble plume area increases with the wave packet slope but there is little difference between the clean water and surfactant-added cases, both in the amount and the persistence of the bubbles. The second peak in these plots (at $t \approx 2$ s) is primarily caused by the rapid upward motion of the free surface that results in the stretching and dilation of the bubble plume (see Figure 4-e). The variations in the plume area values among different runs for $t > 4$ s is due to the residual surface foam appearing in the bubble-plume camera. This contamination of the plume area was reduced through processing and did not affect the correlation with the cooling time, presented below.

The visible foam decay timescale, $\tau_{\text{foam}}^{\text{decay}}$, and the bubble plume decay timescale, $\tau_{\text{plume}}^{\text{decay}}$, for each experimental run were calculated from their corresponding time series. An exponential function in the form of $A_* = A_*^{\text{max}} \exp(-t/\tau_*^{\text{decay}})$, where $*$ = (foam, plume), was fit to the data between the time of maximum area and the time when the area drops below a threshold. The average values of the maximum foam and bubble plume areas for each slope are listed in Table 1. The fitted curve was constrained to include the maximum area data point. The threshold used for the foam time series was 5% of the maximum area. For the plume area time series, the threshold was varied for different wave packet slopes to

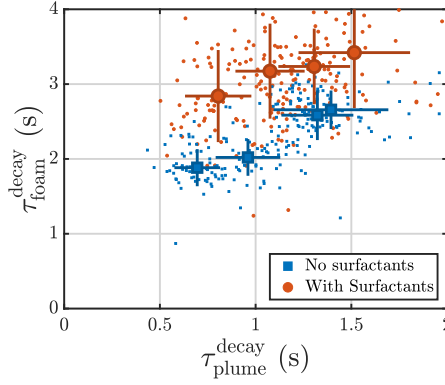


Figure 8. Visible foam timescale $\tau_{\text{foam}}^{\text{decay}}$ versus bubble plume timescale $\tau_{\text{plume}}^{\text{decay}}$. Each small symbol represents one experimental run. The large symbols are the mean value for each wave packet slope S . The error bars show one standard deviations of the samples.

reduce the fitting error due to the influence of the residual foam at the surface, which could be detected as bubble plume by the processing algorithm. The threshold values for these cases were between 0.2 and 0.4 of the maximum plume area. The locations corresponding to the decay of the foam and plume area curves to a value of $1/e$ from their maxima are indicated in Figure 7 by vertical lines for both the surfactant-free and surfactant-added cases. Thus the magnitude of the timescales is given by the time between the maximum and the corresponding vertical line (Figure 6). The difference between the surfactant-free and surfactant-added cases is readily apparent for the visible foam timescale while practically no difference occurs for the plume timescale.

Figure 8 shows that the visible foam timescale $\tau_{\text{foam}}^{\text{decay}}$ increases approximately linearly with the bubble plume decay timescale $\tau_{\text{plume}}^{\text{decay}}$, which is consistent with the results of Callaghan et al. (2013). They found a 1:1 correspondence for surfactant-free conditions, whereas the slope of the surfactant-free correlation for our measurements is approximately 2. While our bubble plume decay times for surfactant-free conditions are comparable to theirs, our foam decay times are about twice as large. Since the foam lifetime is known to be a function of salinity and seawater composition, the most likely reason for the difference in foam decay time and slope is that we used artificial seawater (Instant Ocean) while Callaghan et al. (2013) used filtered natural seawater. We found that adding surfactants increased the foam area decay time by an average of 32%. Furthermore, the slope of the approximately linear behavior with surfactants is comparable to that for surfactant-free conditions. Although Callaghan et al. (2013) also found an increase in foam decay time with surfactants, they reported a significantly larger slope than we found. In addition to the effects of using different types of sea water, another possible difference that could affect the magnitude of the surfactant effect and resulting slope is the unknown level of surfactants that may have been present for the surfactant-free conditions.

The foam temperature anomaly was calculated for each run using the foam mask sequence extracted from the visible foam images (e.g. Figure 4). This mask was then applied to the corresponding frames of the infrared sequence to isolate the regions covered by the foam from the rest of the image. The time series of the mean foam temperature anomaly, T_{foam} , is plotted in Figure 9(a-d) for each experimental condition. Immediately after the start of the breaking process, the foam temperature increases because of the disruption of the cool skin layer. The foam temperature plateaus for a short but significant time and then starts to cool. These plots show that the duration of the plateau in foam temperature increases with the slope of the wave packet and the onset of the cooling of the foam is delayed

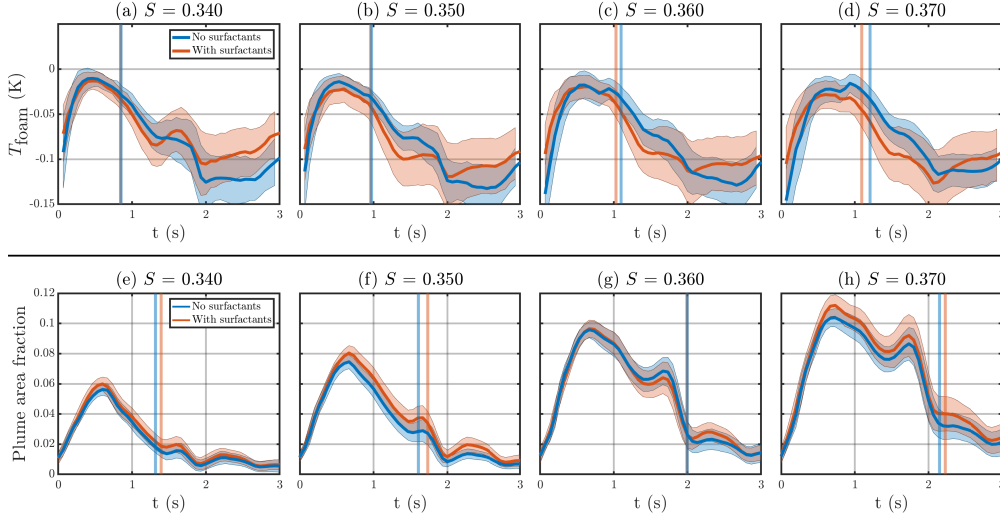


Figure 9. The mean foam temperature anomaly versus time (top) and the bubble plume area (bottom), with and without added surfactants. The thick lines are ensemble averages and the shaded areas denote one standard deviations of the samples. The vertical lines indicate the location t_{cool} for the foam temperature and the e-folding time from the maximum relative to time $t=0$ for the plume area, which is equal to $\tau_{\text{plume}}^{\text{total}}$ (Figure 6).

for the larger breakers compared to the smaller ones. Furthermore, the surfactant-free and surfactant-added cases follow each other closely in these plots. The time series of the bubble plume area from Figure 7(e-h) are repeated in Figure 9(e-h) with the time axis expanded to correspond to the temperature anomaly plots.

Surface foam and subsurface bubbles are generated immediately after the breaking process begins. As shown in Figure 5, the evolution of the thermal signature of foam also commences immediately after breaking starts, beginning as an increase in temperature due to the disruption of the cool skin. Therefore, we define the time to the onset of cooling, t_{cool} , as the time from the start of breaking to when the mean foam temperature anomaly T_{foam} falls below its maximum value by a fixed amount. That amount was taken to be the minimum detectable temperature change given by the noise level of the infrared camera (NEDT of 0.025 K). For comparison of t_{cool} to the bubble plume timescale, we use the total bubble plume timescale, $\tau_{\text{plume}}^{\text{total}} = \tau_{\text{plume}}^{\text{decay}} + t_{\text{plume}}^{\text{max}}$, defined as the bubble plume decay timescale plus the time from the start of breaking to $A_{\text{plume}}^{\text{max}}$, the time of maximum bubble plume area (Figure 6). The use of these timescales based on the time since the beginning of breaking is consistent with the recent approach by Callaghan (2018), who used the sum of the growth and decay phase timescales as the appropriate timescale for determination of whitecap coverage. The onset of cooling and the total bubble plume timescale are indicated in the corresponding time series in Figure 9 by vertical lines for both surfactant-free and surfactant-added cases.

The plot of t_{cool} versus the total bubble plume timescale $\tau_{\text{plume}}^{\text{total}}$ in Figure 10(a) shows an approximately linearly relationship. Small differences in the onset of cooling between the surfactant-free and surfactant-added cases are apparent for the two largest slopes (see also Figure 9(g-h)). However, these differences between the surfactant-free and surfactant-added cases are within the experimental variation, indicated by the standard deviation of the ensemble, and are thus not considered statistically significant. The lack of significant effect of surfactants on t_{cool} is consistent with previous observations that have examined evaporation suppression by surfactant added to water. Some surfactants have the ability to reduce

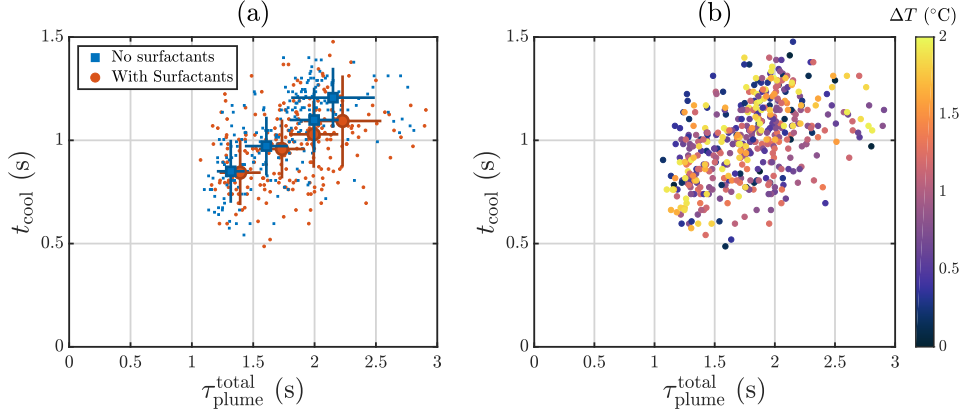


Figure 10. t_{cool} versus $\tau_{\text{plume}}^{\text{total}}$ (a) The small symbols represent individual runs. The large symbols are the ensemble-averaged values at each condition and the error bars show one standard deviations. (b) Each circle represents one experimental run and is colored based on the water-air temperature difference, ΔT , shown in the colorbar.

evaporation through the formation of a monolayer (Barnes, 1986), reducing outward heat flux and suppressing surface cooling. However, this layer is relatively fragile, and mechanical agitation by wind and strong surface turbulence, such as the action of wave breaking and foam generation, will disrupt it and negate any evaporation resistance (Katsaros & Garrett, 1982). The strong and roughly linear correlation between t_{cool} and $\tau_{\text{plume}}^{\text{total}}$ implies that the time to the onset of cooling can be used as a proxy for the total bubble plume timescale without a significant impact of surfactants.

We also examined the effect of the ambient heat flux by varying the air-water temperature difference for each experimental run, shown in Figure 10(b). Each individual data point from Figure 10(a) is colored by the temperature difference between the water and the air, $\Delta T = T_{\text{water}} - T_{\text{air}}$. The lack of a discernible relationship over the two degree range of ΔT , similar to ocean conditions, indicates that the onset of cooling is not strongly affected by the air-water heat flux.

The generated breaking events initially produce a single foam patch and corresponding bubble plume that then quickly separates into two distinct foam patches and bubble plume pairs, as shown in the time sequences from an individual run in Figure 4. The distinct foam patches and associated bubble plumes are generated at different times and with different intensities and thus differ in their spatial and temporal evolution. For instance, the trailing bubble plume in Figure 4(c-e, bottom) is nearly dissipated in Figure 4(f, bottom) when the leading plume is still robust, which is not necessarily reflected in the evolution of the foam patches in the corresponding panels in Figure 4. The occurrence of two separately evolving bubble plumes and corresponding foam patches suggests that separately tracking and measuring the evolution of t_{cool} and $\tau_{\text{plume}}^{\text{total}}$ for one foam-plume pair may improve the correlation.

The analysis region for individual foam patches was identified and tracked using ensemble-averaged intensity images for each slope and surfactant condition, as illustrated by the sequence in Figure 11 (top) for $S = 0.37$ without additional surfactants. Each image is the result of averaging the same frame of foam masks relative to the start of breaking, among all the runs with the same conditions. Therefore, the intensity value at each pixel is equal to the fraction of runs in which the pixel was covered by foam or bubbles. The ensemble averaging of the foam images reveals the well defined two-dimensional structure of the foam. The single transverse strip of foam in Figure 11(a) quickly separates into two transverse strips in

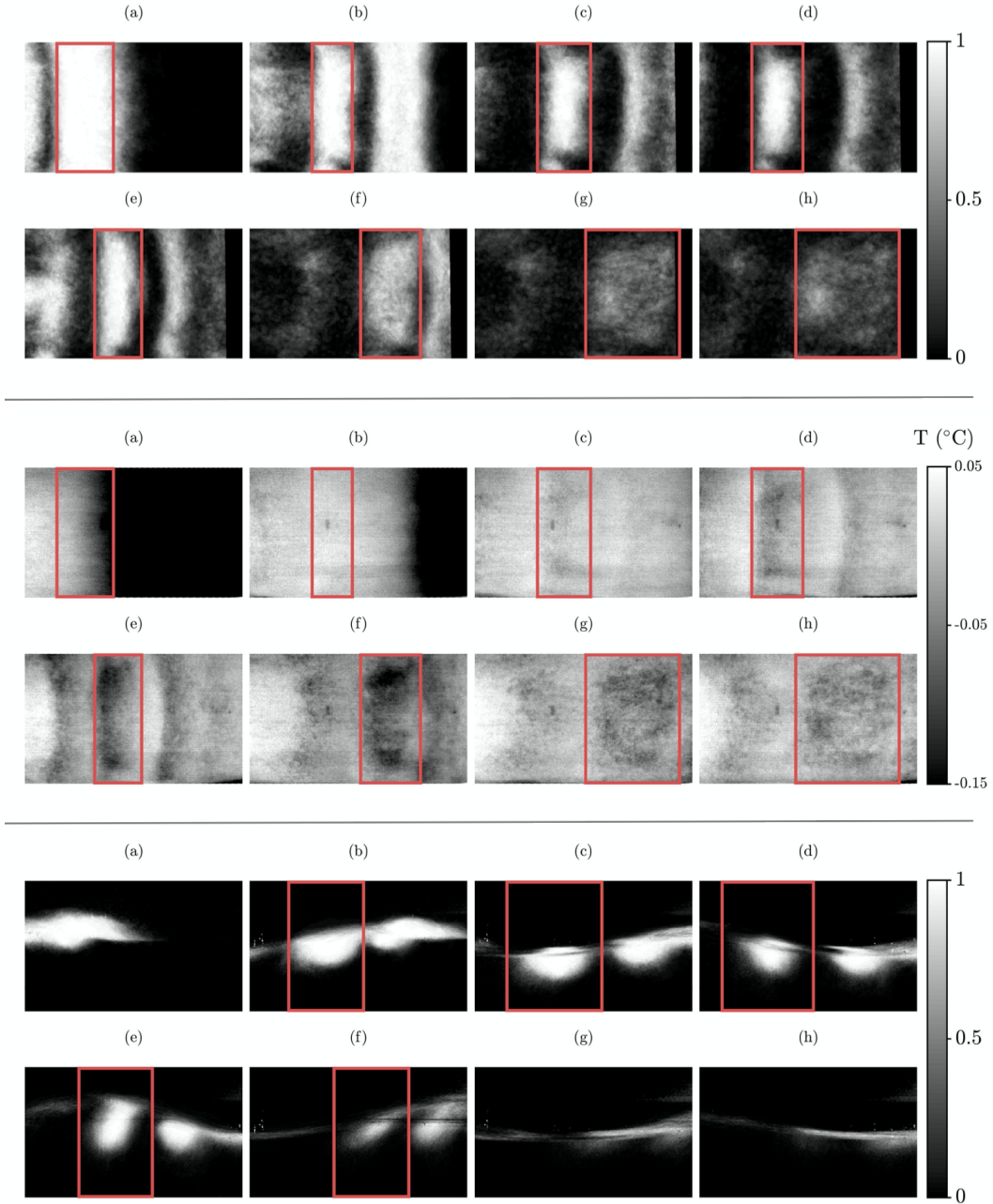


Figure 11. A sequence of ensemble-averaged intensity images of the foam (top), the surface temperature (middle), and the bubble plume (bottom) for the experimental condition with a slope of 0.37 without additional surfactants. The red box follows the most salient foam patch (and the corresponding bubble plume) of the breaker and shows the region that is used in analyzing the foam temperature and the plume area. This figure corresponds to Movie S4 in the supplementary information.

Figure 11(b) that continue to propagate down the tank as separate features. The rectangular box overlaid on each image corresponds to the portion of the image used in analyzing the foam temperature in the individual run sequences of infrared imagery. The location and the

width of the tracking box were defined manually by inspecting the ensemble-averaged foam images with the goal of containing most of the foam in a strip. Note that the tracking boxes were calculated based on the ensemble-averaged foam data and then applied to infrared images from individual runs with the same conditions. The corresponding bubble plume is similarly tracked using the ensemble-averaged bubble plume images (Figure 11, bottom) and then applied to individual runs. The location and width of the tracking window for the bubble plume were defined independently of the tracking window for the foam data. The reason was that the bubble plume is deformed greatly by the fluid motion at depth due to the waves and is not necessarily located directly beneath the foam strip.

The mean temperature of the foam in the tracking box is plotted versus time in Figure 12(a-d). Similar to the results of Figure 9 for the whole field of view, the onset of cooling of the foam is delayed with the scale of the breaking strength, given by the wave packet slope, S . The difference between the surfactant-free and surfactant-added cases is once again relatively small. The bubble plume was similarly tracked as shown in Figure 11 (bottom). However, obtaining the time scale for individual bubble plumes proved to be problematic for the cases with the two larger slopes. The reason for this issue can be seen in the plume area time series shown in Figure 12(e-h). The individual bubble plume could only be tracked up to $t = 2$ s since the separate plumes merged together at that point. Fitting an exponential function to the plume area time series resulted in noisy data due to the lack of data at later stages of decay and the presence of a local peak in the time series caused by the stretching of the bubble plume. However, as can be seen in these plots, the time series for an individual plume follows a trend similar to that for the whole image. Therefore, the maximum depth of the plume, d_{\max} is used instead of $\tau_{\text{plume}}^{\text{total}}$ to present the result of tracking an individual plume. The average values of the maximum bubble plume depth for each slope are listed in Table 1.

Figure 13(a) and 13(b) show the time to the onset of cooling, t_{cool} , versus maximum depth of the plume for the whole field of view (i. e., both plumes) and for tracking the trailing plume, respectively. For both cases, t_{cool} scales with d_{\max} and the difference between the two surfactant conditions is small (approximately 5% on average). Moreover, the scatter of t_{cool} data is less when an individual foam patch was tracked compared to the whole field of view (approximately 0.12 s compared to 0.16 s, respectively). The reduced scatter when tracking a single plume suggests that the spatial variation in T_{foam} is related to the spatial variability of the bubble plume depth.

The correlation of the bubble plume depth with the time to the onset of breaking and the observed spatial variability of the foam temperature anomaly suggest that our technique may provide a means of remotely mapping the spatial variability of the plume depth. Our measurement of the bubble plume timescale and depth provide a global measure of the plume characteristics that include a wide range of bubble sizes. However, the delay of the onset of cooling due to the renewal of the foam by rising bubbles is likely associated with a limited range of larger bubble sizes. The onset of cooling may occur because this subset of bubbles responsible for generating the foam are no longer present. Measurements of the distribution of bubble sizes and their subsurface spatial variability combined with infrared temperature maps would be necessary to confirm this implication of our results.

5 Conclusions

We presented an experimental investigation of the thermal signature of the residual foam left behind by breaking waves. The experiments were conducted in a saltwater wave tank and breaking waves were generated using the dispersive focusing wave packet technique. We used four different wave packets that had a similar shape but varied significantly in breaking intensity, plume depth, and energy dissipation. For each packet, more than a hundred experiment runs were performed in salt water with and without added surfactants. The visible and thermal signatures of the surface foam produced by the breaking waves

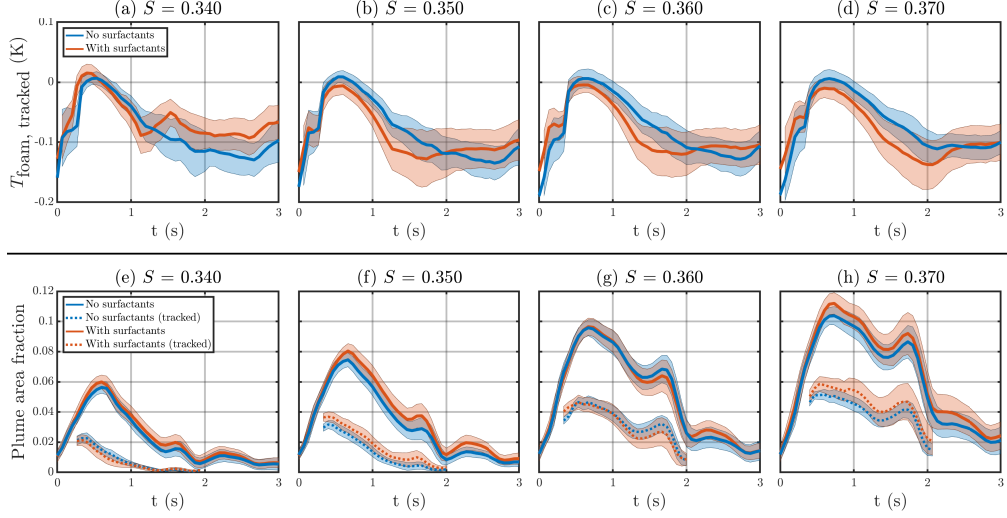


Figure 12. (Top) the mean foam temperature anomaly in the tracking box versus time, with and without additional surfactants. Thick lines are ensemble averages and the shaded areas are one standard deviations of samples. (Bottom) bubble plume area normalized by the image size. Solid lines are for the whole field of view and dotted lines are the data inside the tracking window.

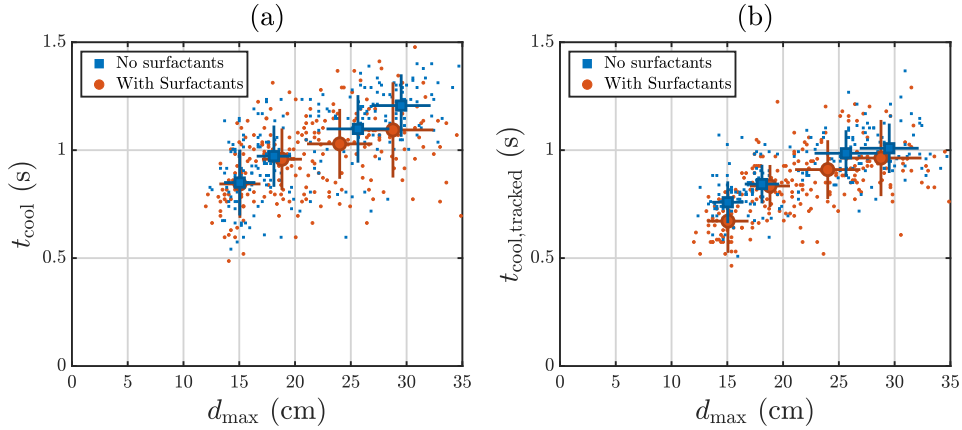


Figure 13. t_{cool} versus the maximum depth of the plume, d_{max} (a) without tracking, and (b) with tracking. The small symbols represent individual runs. The large symbols are the ensemble-averaged values at each condition and the error bars show one standard deviations.

were measured. The foam area, bubble plume area, and foam temperature time series were calculated from the image sequence data for each experimental run. The visible foam timescale, $\tau_{\text{foam}}^{\text{decay}}$, the bubble plume time scales $\tau_{\text{plume}}^{\text{decay}}$ and $\tau_{\text{plume}}^{\text{total}}$, and the time to the onset of cooling, t_{cool} , were evaluated from their corresponding time series.

The time to the onset of cooling of the foam, t_{cool} , was found to scale with the total plume decay time, $\tau_{\text{plume}}^{\text{total}}$, and the maximum plume depth. The cooling timescale was not significantly affected by the environmental conditions of surfactant concentration and air-water temperature difference. Therefore, t_{cool} can be used to infer sub-surface plume dynamics by quantifying the plume decay time and depth from sea surface temperature observations.

Our results are consistent with the laboratory result that surface foam cools faster than the surrounding clear water due to the enhanced cooling of the bubbles at the surface. Furthermore, they support the notion that the cooling of surface foam is delayed until the rate of renewal of the foam by rising bubbles is less than the foam cooling rate. Our results suggest that the observed spatial variability of T_{foam} (Figure 5) may provide information about the spatial variability of the bubble plume depth. Adequate investigation of this idea will require additional measurements with increased dynamic range of breaking intensity and techniques to quantify spatial variability of the bubble plume depth.

Acknowledgments

This work was supported by the National Science Foundation through grant number OCE-1736504 and the APL-UW SEED postdoctoral program. We acknowledge Mr. Joseph Zacharin for assisting with the experiments, APL Ocean Engineering for engineering and modification of WASIRF, and Dr. Morteza Derakhti for helpful discussions. The data underlying this paper can be found at this address: <http://hdl.handle.net/1773/45571>.

References

- Anguelova, M. D., & Webster, F. (2006). Whitecap coverage from satellite measurements: A first step toward modeling the variability of oceanic whitecaps. *Journal of Geophysical Research: Oceans*, 111(C3).
- Barnes, G. (1986). The effects of monolayers on the evaporation of liquids. *Advances in Colloid and Interface Science*, 25, 89 - 200.
- Callaghan, A. H. (2013). An improved whitecap timescale for sea spray aerosol production flux modeling using the discrete whitecap method. *Journal of Geophysical Research: Atmospheres*, 118(17), 9997-10,010.
- Callaghan, A. H. (2018). On the relationship between the energy dissipation rate of surface-breaking waves and oceanic whitecap coverage. *Journal of Physical Oceanography*, 48(11), 2609-2626.
- Callaghan, A. H., Deane, G. B., & Stokes, M. D. (2008). Observed physical and environmental causes of scatter in whitecap coverage values in a fetch-limited coastal zone. *Journal of Geophysical Research: Oceans*, 113(C5).
- Callaghan, A. H., Deane, G. B., & Stokes, M. D. (2013). Two regimes of laboratory whitecap foam decay: Bubble-plume controlled and surfactant stabilized. *Journal of Physical Oceanography*, 43(6), 1114-1126.
- Callaghan, A. H., Deane, G. B., & Stokes, M. D. (2017). On the imprint of surfactant-driven stabilization of laboratory breaking wave foam with comparison to oceanic whitecaps. *Journal of Geophysical Research: Oceans*, 122(8), 6110-6128.
- Callaghan, A. H., Deane, G. B., Stokes, M. D., & Ward, B. (2012). Observed variation in the decay time of oceanic whitecap foam. *Journal of Geophysical Research: Oceans*, 117(C9).
- Callaghan, A. H., & White, M. (2009). Automated processing of sea surface images for the determination of whitecap coverage. *Journal of Atmospheric and Oceanic Technology*, 26(2), 383-394.
- Carini, R. J., Chickadel, C. C., Jessup, A. T., & Thomson, J. (2015). Estimating wave energy dissipation in the surf zone using thermal infrared imagery. *Journal of Geophysical Research: Oceans*, 120(6), 3937-3957.
- Chickadel, C. C., Branch, R., & Jessup, A. T. (2014). Thermal infrared signatures and heat flux of sea foam. *American Geophysical Union, Ocean Sciences Meeting*.
- Deane, G., & Stokes, M. (2002). Scale dependence of bubble creation mechanisms in breaking waves. *Nature*, 418, 839-44.
- Drazen, D. A., Melville, W. K., & Lenain, L. (2008). Inertial scaling of dissipation in unsteady breaking waves. *Journal of Fluid Mechanics*, 611, 307-332.
- Duncan, J. H., Qiao, H., Philomin, V., & Wenz, A. (1999). Gentle spilling breakers: crest

- profile evolution. *Journal of Fluid Mechanics*, 379, 191-222.
- Erinin, M. A., Wang, S. D., Liu, R., Towle, D., Liu, X., & Duncan, J. H. (2019). Spray generation by a plunging breaker. *Geophysical Research Letters*, 46(14), 8244-8251.
- Evans, J., Stride, E., Edirisinghe, M., Andrews, D., & Simons, R. (2010). Can oceanic foams limit global warming? *Climate Research*, 42, 155-160.
- Fogelberg, R. (2003). *A study of microbreaking modulation by ocean swell using infrared and microwave techniques* (Unpublished master's thesis). University of Washington.
- Gordon, H. R., & Jacobs, M. M. (1977). Albedo of the ocean-atmosphere system: influence of sea foam. *Applied Optics*, 16(8), 2257-2260.
- Goshtasby, A. (1986). Piecewise linear mapping functions for image registration. *Pattern Recognition*, 19(6), 459 - 466.
- Jessup, A. T., Zappa, C. J., Loewen, M. R., & Hesany, V. (1997). Infrared remote sensing of breaking waves. *Nature*, 385(6611), 52-55.
- Katsaros, K. B., & Garrett, W. D. (1982). Effects of organic surface films on evaporation and thermal structure of water in free and forced convection. *International Journal of Heat and Mass Transfer*, 25(11), 1661 - 1670.
- Kiger, K. T., & Duncan, J. H. (2012). Air-entrainment mechanisms in plunging jets and breaking waves. *Annual Review of Fluid Mechanics*, 44(1), 563-596.
- Kleiss, J., & Melville, W. (2010). Observations of wave breaking kinematics in fetch-limited seas. *Journal of Physical Oceanography*, 40, 2575-2604.
- Lamarre, E., & Melville, W. (1991). Air entrainment and dissipation in breaking waves. *Nature*, 351, 469-472.
- Loewen, M. R. (1991). *Laboratory measurements of the sound generated by breaking waves* (Unpublished doctoral dissertation). MIT/WHOI Joint Program.
- Marmorino, G. O., & Smith, G. B. (2005). Bright and dark ocean whitecaps observed in the infrared. *Geophysical Research Letters*, 32(11).
- Monahan, E. C. (1969). Fresh water whitecaps. *Journal of the Atmospheric Sciences*, 26(5), 1026-1029.
- Monahan, E. C., & Lu, M. (1990). Acoustically relevant bubble assemblages and their dependence on meteorological parameters. *IEEE Journal of Oceanic Engineering*, 15(4), 340-349.
- Monahan, E. C., Spiel, D. E., & Davidson, K. L. (1986). A model of marine aerosol generation via whitecaps and wave disruption. In E. C. Monahan & G. M. Niocaill (Eds.), *Oceanic whitecaps: And their role in air-sea exchange processes* (pp. 167-174). Dordrecht: Springer Netherlands.
- Potter, H., Smith, G. B., Snow, C. M., Dowgiallo, D. J., Bobak, J. P., & Anguelova, M. D. (2015). Whitecap lifetime stages from infrared imagery with implications for microwave radiometric measurements of whitecap fraction. *Journal of Geophysical Research: Oceans*, 120(11), 7521-7537.
- Rapp, R. J., & Melville, W. K. (1990). Laboratory measurements of deep-water breaking waves. *Philosophical Transactions of the Royal Society of London. Series A, Mathematical and Physical Sciences*, 331(1622), 735-800.
- Scanlon, B., & Ward, B. (2013). Oceanic wave breaking coverage separation techniques for active and maturing whitecaps. *Methods in Oceanography*, 8, 1 - 12.
- Veron, F. (2015). Ocean spray. *Annual Review of Fluid Mechanics*, 47(1), 507-538.
- Wang, A., Ikeda-Gilbert, C. M., Duncan, J. H., Lathrop, D. P., Cooker, M. J., & Fullerton, A. M. (2018). The impact of a deep-water plunging breaker on a wall with its bottom edge close to the mean water surface. *Journal of Fluid Mechanics*, 843, 680-721.

Supporting Information for “On the Thermal Signature of the Residual Foam in Breaking Waves”

N. Masnadi¹, C. C. Chickadel¹, and A. T. Jessup¹

¹Applied Physics Lab, University of Washington

Additional Supporting Information (Files uploaded separately)

Caption for Movies S1 to S4:

Movie S1 and Movie S2. A sequence of images of a breaking wave with a slope of $S = 0.35$ for Movie S1 and $S = 0.37$ for Movie S2. Movie S2 corresponds to the images in Figure 3 and Figure 7 in the paper. The movies are captured and played at 15 fps. The wave is propagating from left to right. The wave packets are designed so that the breaking occurs at the edge of the field of view. (Left) Bubble plume images taken from the camera that is looking through the glass wall of the tank. (Top right) Visible foam images taken by the camera that is looking down at the water surface. The foam images are shown in the same coordinate system as of the infrared camera images. (Bottom right): infrared images showing the surface temperature of the foam. The temperature range is $0.3\text{ }^{\circ}\text{C}$ with dark meaning cold and bright meaning warm. The blue outlines show the location of the foam extracted from the visible foam images. Each image is approximately 1.2 m long.

Movie S3 and Movie S4. A sequence of ensemble-averaged intensity images of the bubble plume (left), the foam (top right), and the surface temperature (bottom right), for the experimental condition with a slope of $S = 0.35$ in Movie S3 and $S = 0.37$ for Movie S4. Movie S4 corresponds to the images in Figure 10 in the paper. The movies are captured and played at 15 fps. Each frame in the foam (bubble plume) movies is the result of averaging the same frame of foam masks (bubble plume mask) relative to the start of breaking, among all the runs with the same conditions. Therefore, the intensity value at each pixel is equal to the fraction of runs in which the pixel was covered by foam (bubbles). Similarly, the infrared movie is the result of ensemble averaging of all the runs with the same condition. The temperature range in the infrared movie is $0.2\text{ }^{\circ}\text{C}$ with dark meaning cold and bright meaning warm.